Editors' Suggestion | Featured in Physics

Traveling Perversion as Constant Torque Actuator

Émilien Dilly,[1] Sébastien Neukirch,[2] Julien Derr,[3] and Dražen Zanchi[1,*]
[1]Laboratoire Matière et Systèmes Complexes, UMR 7057, Université Paris Cité, CNRS, F-75205 Paris Cedex 13, France
[2]Institut Jean Le Rond d'Alembert, CNRS (UMR 7190), Sorbonne Université, 75005 Paris, France
[3]Laboratoire Reproduction et Développement des Plantes, École Normale Supérieure de Lyon, CNRS, INRAE, Inria, 69364 Lyon Cedex 07, France

(Received 8 April 2023; revised 19 August 2023; accepted 15 September 2023; published 24 October 2023)

Mechanical stress and conformation of helical elastic rods clamped at both ends were studied upon unwinding. By axial rotation of one end, the winding number was progressively changed from the natural one ($n = n_0$) to complete chirality inversion ($n = -n_0$) while keeping the total elongation fixed and monitoring the applied torque M and tension T. Along the unwinding process, the system crosses three distinct states: natural helix (+), mixed state (+/−), and inverted helix (−). The mixed state involves two helices with opposite chiralities spatially connected by a perversion (helicity inversion). Upon unwinding, the perversion is "injected" (nucleated) from one side and travels toward the opposite side where it is eventually "absorbed" (annihilated), leaving the system in the (−) state. In the mixed state, the profile of $M(n)$ is almost flat: the system behaves as a constant torque actuator. The three states are quantitatively well described in the framework of a biphasic model which neglects the perversion energy and finite size effects. The latter are taken into account in a numerical simulation based on the Kirchhoff theory of elastic rods. The traveling perversion in helical elastic rods and related topological phenomena are universal, with applications from condensed matter to biological and bioinspired systems, including in particular mechanical engineering and soft robotics.

DOI: 10.1103/PhysRevLett.131.177201

An unloaded elastic rod with uniform curvature and twist adopts a helical shape with radius R_0 and pitch χP_0, with chirality $\chi = \pm 1$ for a positively or negatively turning helix, corresponding to positive or negative winding number n_0. If the rod is now held by its ends and twisted so that the total winding number n becomes zero, its shape then comprises two helices with opposite handedness separated by a perversion, a phenomenon relevant to a number of biological and bioinspired systems including tendrils of plants [1,2], propelling flagella of microorganisms [3,4], and even electrospun microfibrils [5,6]. The interest for twisted elastic rods [7–9] was renewed in the last decades [10,11] in the context of single molecule DNA nanomechanics [12–17], plant development [18,19], soft robotics, or microengineering [20–22], and these applications have in turn motivated theoretical research [23–28]. A theoretical description of helical elastic rods using the formalism of dynamical systems provides an explanation for the winding of tendrils of plants with single or multiple perversions [29–31]. An analogy between perversion and fractional charges in Haldane's dimerized quantum spin chain was also recently proposed [28].

Continuous handedness inversion of an elastic helix is, to our knowledge, still an open question. To reverse the chirality of a helix with $n = n_0$, one can start to unwind it at constant elongation [see Fig. 1(a) and the Supplemental Material [32], video 1]. At some critical winding $0 < n < n_0$ a perversion is generated at one end, in agreement with theoretical prediction [28]. As unwinding continues, the injected perversion travels toward the opposite end. Finally, at another critical winding $-n_0 < n < 0$, the perversion gets "absorbed" at the opposite end, and we obtain a purely hand-reversed helix. If now the stretching force is relieved, the elongation decreases and the obtained hand-reversed helix adopts a conformation where the coils are collapsed, maintained by contact forces (see the Supplemental Material [32], Fig. S1). The generation (injection) and the absorption (expulsion) of the perversion are singular events, reminiscent of phase transitions. Their experimental and theoretical quantification is a delicate issue, as it will be discussed.

In this Letter, we report on experiments, theory, and simulation of chirality inversion of elastic helices clamped at both ends at extension z and winding n. The resulting phase diagram in the (z, n) space for three encountered phases, the natural chirality helix (+), the coexistence of both chiralities (+/−), and the opposite chirality (−), is shown in Fig. 1(b). We also monitored the axial torque M and axial force T as functions of n, from $n = n_0$ to $n = -n_0$; see Fig. 2. The phase diagram is reproduced within a model based on phase coexistence of (+) and (−) chirality helices ignoring clamped boundaries and the perversion. In order to take into account the perversion itself and the boundary conditions, we performed numerical

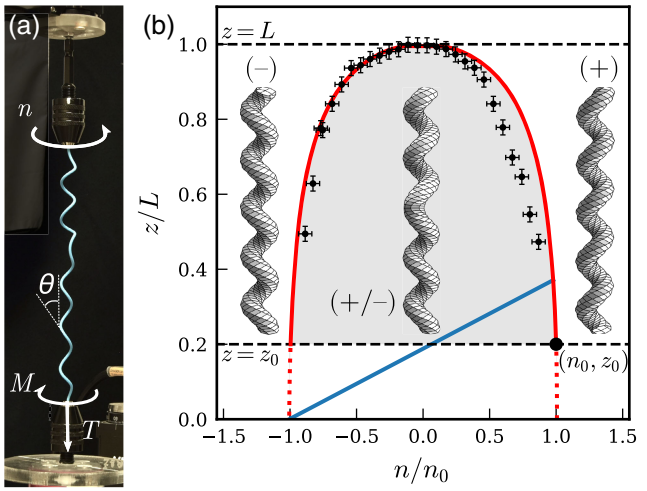

FIG. 1. (a) Experimental setup. The rod is held by mandrels at its extremities; the upper mandrel is rotated n turns while the lower mandrel is fixed to a torque meter and a scale. The mandrels apply a torque $\mathbf{M}$ and a force $\mathbf{T}$ on the rod. (b) Experimental phase diagram in the (z, n) plane for the parameter value $z_0/L = 0.2$, where L is the total length. The regions $(-)$, $(+/-)$, and $(+)$ correspond respectively to reversed chirality, the coexistence of both chiralities, and natural chirality. The dotted horizontal line for $z = z_0$ represents the value of z of the unloaded helix, so that for $z > z_0$ (shaded) the helix is extended. The black crosses are experimental data, and the red curve is the calculated phase boundary with the biphasic model; see the Supplemental Material [32], data 1. The blue line is the calculated limit below which the $(-)$ part of the rod has loops collapsed in self-contact; see the Supplemental Material [32], video 2. The black dot indicates the natural state of the helix (n_0, z_0).

simulations on a finite-size system in the Kirchhoff model, reproducing in detail both $M(n)$ and $T(n)$ profiles, including oscillations, a pseudoplateau of $M(n)$, and jumps at both ends of the mixed phase; see Fig. 3.

We report data for elastomer helical rods with Young's modulus $E = 5.0 \pm 2$ MPa, radius $R_0 = 3.9$ mm, pitch $P_0 \equiv z_0/n_0 = 4.7$ mm, thickness $d = 1.7$ mm, and $n_0 = 9.5$; see the Supplemental Material [32] for more details. For the sake of verification, experiments with several helices with different radii and pitches were also carried out. Fig. 1(a) shows the experimental setup where the rod is clamped in a mandrel at each end. The upper end is fixed to a rotation stage while the lower end is connected to both a torque meter and a force gauge.

Figure 1(b) shows domains of existence in (extension vs winding number) plane, for the states $(+)$, $(-)$, and the mixed state $(+/-)$ where the system comprises both $(+)$ and $(-)$ regions together with a perversion at the interface between them. The extension z and the winding number n are normalized respectively by the total arclength L and by the number of coils of the unloaded rod n_0. The boundary between the different phases is determined experimentally by increasing z at constant n starting from the $(+/-)$ state.

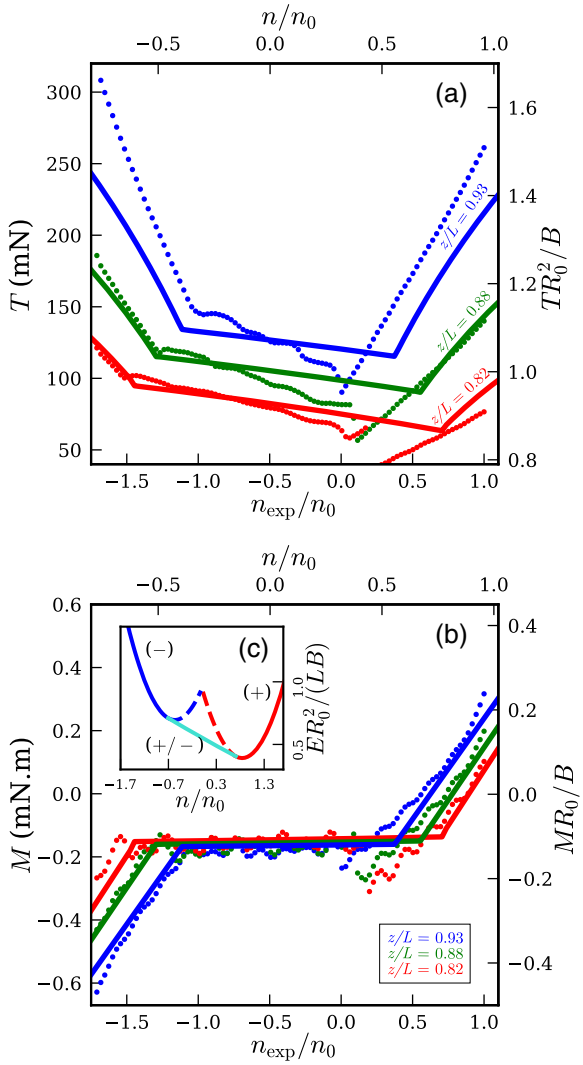

FIG. 2. Profiles of the force $T(n)$ (a) and torque $M(n)$ (b) for $n_0 = 9.5$ coils and $z_0/L = 0.2$. Different values of the elongation z are used: blue, $z/L = 0.93$; green, $z/L = 0.88$; red, $z/L = 0.82$. Dots are measured quantities, and thick lines are quantities calculated in the biphasic approximation for a rod with Poisson ratio $\nu = 0.5$. Inset (c) shows the strain energy calculated separately for all three phases for $z/L = 0.82$. The physical solution corresponds to the minimal one at given n.

At a critical z, the perversion disappears (with a corresponding slope discontinuity on the axial torque), yielding either a pure $(+)$ or $(-)$ state, depending on the sign of n. The width of the coexistence zone over n decreases as z gets larger, meaning that the more elongated the helix is, the more one needs to unwind to inject a perversion. In the limit $z \to L$, the value of n at which the perversion appears goes to 0: for a completely straight rod, a perversion cannot exist. On the other hand, as z goes down to z_0 (the extension of unloaded rod), the width of the coexistence zone increases. In the biphasic model (discussed below), at $z = z_0$, coexistence happens for $-1 \lesssim n/n_0 \leq +1$ which means that if one starts with the natural

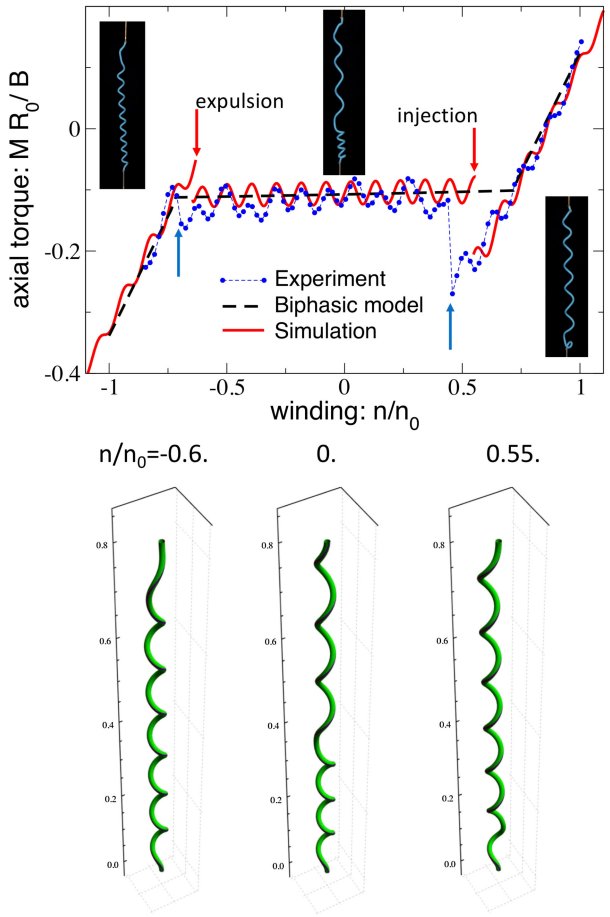

FIG. 3. Experimental profile $M(n)$ compared to numerical simulations and biphasic calculations, with no fitting parameter. The parameters for simulation are $z_0/L = 0.2$, $z/L = 0.82$, and $n_0 = 9.5$. The events of creation and annihilation of the perversion are pointed by arrows, blue for experiment and red for simulation. The snapshots of the rod at these events and in the mixed state are shown in insets. Calculated configurations for the three cases are shown on the lower panel.

state ($n/n_0 = 1 = z/z_0$), any unwinding would lead to the presence of a perversion.

Figure 2 shows typical results of helix unwinding experiments for three values of z. The overall mechanical behavior of the rod is qualitatively similar at any z. The unwinding experiments start at $n/n_0 = 1$ with (+) chirality. As n decreases, M decreases, and the axial force T decreases. At a critical n, a snapping transition occurs, and a perversion is created at one extremity of the rod. The choice of the snapping extremity is arbitrary. For lower n values, a regime takes place where (+) and (−) helices coexist, connected by a perversion. Moreover, depending on z, the snapping occurring at the creation of a perversion is accompanied by a self-contact between the (−) coils; see the Supplemental Material [32], video 1. Within this mixed state (+/−), T increases and M exhibits a pseudoplateau, the plateau value depending on z and z_0. As n is further decreased, the perversion disappears at the opposite end, M decreases again, and T continues to increase, but with a steeper slope. This latter regime corresponds to a pure (−) helix with chirality opposite to the natural one. The jump in $M(n)$ is weaker at this side of the plateau, when the perversion gets annihilated. The oscillations, occurring once per turn, are clearly visible in $M(n)$ and, albeit to a lesser extent, in $T(n)$.

To reproduce the phase diagram and the profiles of $T(n)$ and $M(n)$, we use a biphasic approximation in which we neglect the perversion and the boundary layers near the clamps; this simplification holds true in the limit $n_0 \to \infty$. We therefore work with the elastic energy

$$E(\kappa_\pm, \tau_\pm, \alpha) = \alpha L \epsilon_+ + (1-\alpha) L \epsilon_-, \tag{1}$$

where α and $(1-\alpha)$ are the fractions of rod in the (+) and (−) chirality states respectively. In the Kirchhoff approximation [8,30], which assumes that the rod is inextensible, unshearable, and has a constant cross section, linear densities of energy $\epsilon_\pm$ are written as

$$\epsilon_\pm = \frac{1}{2} B (\kappa_\pm - \kappa_0)^2 + \frac{1}{2} C (\pm\tau_\pm - \tau_0)^2, \tag{2}$$

where B and C are the bending and the twisting stiffnesses. For a homogeneous and isotropic material quantities B and C are given by $B = EI$ and $C = EI/(1+\nu)$, where $I = \pi d^4/64$ is the second moment of the circular cross section, ν the Poisson ratio, and E the Young modulus. The quantities $\kappa_\pm$ and $\tau_\pm$ are respectively the curvature and the torsion in the equilibrium chiral states $\chi = \pm 1$, and κ_0 and τ_0 are their values in the natural (unloaded) state. In our notation the torsions $\tau_\pm$ of both (+) and (−) states are positive. Curvatures are related to radii R_i and pitches P_i by $\kappa_i = R_i/[R_i^2 + (P_i^2/4\pi^2)]$ and $\tau_i = (|P_i|/2\pi)/[R_i^2 + (P_i^2/4\pi^2)]$, where i stands for +, − or 0.

The energy (1) is minimized under fixed elongation ζ and winding number μ

$$\zeta = \alpha L \frac{\tau_+}{\sqrt{\kappa_+^2 + \tau_+^2}} + (1-\alpha) L \frac{\tau_-}{\sqrt{\kappa_-^2 + \tau_-^2}} = z \tag{3a}$$

$$\mu = \alpha \frac{L}{2\pi} \sqrt{\kappa_+^2 + \tau_+^2} - (1-\alpha) \frac{L}{2\pi} \sqrt{\kappa_-^2 + \tau_-^2} = n. \tag{3b}$$

The conformation of the rod at given z and n is then found by introducing the Lagrangian

$$\mathcal{L} = E - T(\zeta - z) - 2\pi M(\mu - n)$$

where T and M are the Lagrange multipliers associated with the constraints (3), and are recognized as the axial force and axial torque applied on the system. This variational approach has then seven unknowns: $\kappa_\pm$, $\tau_\pm$, α, T, and M. Requiring $\partial\mathcal{L}/\partial\kappa_\pm = 0$ and $\partial\mathcal{L}/\partial\tau_\pm = 0$ yields

$$\frac{T}{B} = \gamma_+\tau_+\sqrt{\kappa_+^2+\tau_+^2} = \gamma_-\tau_-\sqrt{\kappa_-^2+\tau_-^2}, \tag{4a}$$

$$\frac{M}{B} = (\kappa_+^2+\tau_+^2)^{-1/2}[\kappa_+(\kappa_+-\kappa_0)+\Gamma\tau_+(\tau_+-\tau_0)] \tag{4b}$$

$$= -(\kappa_-^2+\tau_-^2)^{-1/2}[\kappa_-(\kappa_--\kappa_0)+\Gamma\tau_-(\tau_-+\tau_0)], \tag{4c}$$

where we have used the notations $\gamma_\pm = \kappa_0/\kappa_\pm - 1 + \Gamma(1 \mp \tau_0/\tau_\pm)$ and $\Gamma = C/B = 1/(1+\nu)$. The equations (4) corroborate the conservation of force T and torque M along the rod, and are equivalent to the conserved quantities $I_2 \equiv \mathbf{T}^2$ and $I_3 \equiv \mathbf{M}\cdot\mathbf{T}$ [30], with $\mathbf{T} = (0,0,T)$ and $\mathbf{M}\cdot\mathbf{T}/T = M$.

In the cases $\alpha = 0$ or $\alpha = 1$, corresponding to purely (+) and (−) configurations, $\kappa_\pm$ and $\tau_\pm$ are found from (3). The loads T and M are given by (4), and the energy by (1). When computing the profiles of Fig. 2, we need to compare the energy of the purely (+) and (−) states to the energy of the mixed state, i.e., when $0 < \alpha < 1$. The value of α is fixed by setting $\partial\mathcal{L}/\partial\alpha = 0$ which yields

$$\kappa_+^2 + (\Gamma+2\gamma_+)\tau_+^2 = \kappa_-^2 + (\Gamma+2\gamma_-)\tau_-^2, \tag{5}$$

which is, interestingly, equivalent to conservation of the invariant $I_1 \equiv \kappa_1^2+\kappa_2^2+\Gamma\kappa_3^2+2\mathbf{T}\cdot\mathbf{d_3}/B$, with $\mathbf{d_3}$ the tangent to the rod [33].

The seven equations, (3), (4), and (5), are solved numerically for the seven unknowns, κ_+, κ_-, τ_+, τ_-, T, M, and α. For the mixed state, we only keep solutions having $0 < \alpha < 1$. For these solutions, the energy is always found to be lower than the energy of the pure (+) and (−) states: as soon as it exists the mixed state prevails. The phase diagram of Fig. 1(b) is drawn for $z_0/L = 0.2$ and shows for which values of z/L and n/n_0 each of the three states [(+), (−), or mixed] prevails. The red line corresponds to either $\alpha = 0^+$ or $\alpha = 1^-$ and represents the calculated boundary in the $(n/n_0, z/L)$ plane where the mixed state becomes energetically favorable. The blue line represents the occurrence of $\tau_- = 0$ within the mixed phase. Below this line, the numerical solution for the (−) segment has a negative extension. Physically, the (−) segment remains in self-contact during experiments, since it cannot adopt a negative extension due to contact between coils; see the Supplemental Material [32], video 2. Calculated profiles $M(n)$ and $T(n)$ are shown in Fig. 2.

The model captures the overall features found in experiments. In particular, the average value of the pseudoplateau is approximately

$$M_{\text{plateau}} \approx -B\Gamma z z_0\sqrt{1-(z_0/L)^2}/(R_0L^2) \tag{6}$$

while deviation from this constant is $\Delta M \equiv M(\alpha = 1^-) - M(\alpha = 0^+) \approx 2.5B\Gamma(1-z/L)z_0^2/(R_0L^2)$, indicating that for z close to L and z_0/L small (weak natural torsion), the slope of the plateau can be neglected compared with M_{plateau}. In our case, where $z_0/L = 0.2$ and for $z/L > 0.8$, we have $M_{\text{plateau}}/\Delta M \gtrsim 10$. Therefore, in what follows we omit the prefix "pseudo" and use the term "plateau." Notice that M_{plateau} scales with the twisting stiffness C and z_0, related to τ_0 via $z_0/L = \tau_0/\sqrt{\kappa_0^2+\tau_0^2}$. This means that during inversion, one has to provide work against the natural torsion of the helix in order to invert the pitch. When $z/L \to 1$ the transition line (red line in Fig. 1) has a parabolic shape $n \approx \sqrt{1-(z/L)^2}h(\Gamma, z_0/L, z/L)$ where the function h is of order 1. The corresponding force at transition reads as $T \approx B[1-(z_0/L)^2]^{3/2}h(\Gamma, z_0/L, z/L)/R_0^2$ and the torque $M \approx -B\Gamma z_0\sqrt{1-(z_0/L)^2}/(R_0L)$. These formulas remind us that the transition at $z = L$ (usually called the *writhing* transition) happens at a *finite* load, and generalize the critical load value given in [30].

There is a shift in the value of n between experiment (upper abscissa labels) and theory (lower abscissa labels); see Fig. 2. This shift is a manifestation of some memory effects [34] that our theory, based on linearly elastic and unshearable rods, does not capture. In the experiment, the memory effects can be avoided if one chooses vertical trajectories in (n, z) space as we did for constructing the phase diagram [Fig. 1(b)].

We now focus on experimental features not captured by the biphasic approximation: the jumps in M at the injection and expulsion of the perversion and the oscillations in $M(n)$. The surplus of axial torque necessary to inject the perversion is due to the energy barrier necessary for the nucleation of the perversion. The analytical biphasic model does not take into account this energy barrier, and this explains why the values of n at which the perversion appears do not concur in Figs. 1(b) and 2: one has to unwind further in order to provide enough energy to overcome the nucleation barrier. The jump in M at the disappearance of the perversion is far less pronounced: indeed, the left side of experimental and theoretical profiles coincide fairly in Figs. 1(b) and 2(b).

In order to capture the finite-size effects due to the perversion and the boundaries, we carried out numerical simulations of a Kirchhoff elastic rod, using AUTO07 [35]; see the Supplemental Material [32]. The results for $M(n)$ at fixed elongation $z/L = 0.82$ are shown in Fig. 3 and compared to both experiments and the biphasic model. The entire simulated n evolutions of M including the shapes of the clamped rods with $n_0 = 9.5$ and $n_0 = 4$ are shown in the Supplemental Material [32], videos 3 and 4 respectively. The discontinuities at injection and expulsion of the perversion are recovered with fair precision, as well as the oscillations. Notice from the video that the jump at injection and at expulsion as well as the amplitude of oscillations decrease with increasing n_0, as expected [34]. The simulation also captures the asymmetry between the creation and annihilation jumps, resulting from the fact that

the state of inverse chirality is energetically higher than the original one because of the positive natural chirality τ_0; see Eq. (2). This asymmetry also explains why the value of the plateau in M is not zero.

The oscillations of the axial torque during the coexistence regime are linked to the clamping boundary conditions. Recall that in the biphasic model, where conformations are purely helical, these oscillations are absent. Clamping conditions are incompatible with pure helical shapes because the conformation near the clamp cannot be a helix. Therefore, by constraining the rod to be clamped at opposite ends, we introduce some axial asymmetry which results in the observed oscillations.

Being a boundary between two demixed phases, the perversion can be seen as a soliton. In a rod with natural curvature $\kappa_0 > 0$ but no natural torsion ($\tau_0 = 0$), the two states (+) and (−) would be completely symmetric, i.e., energetically degenerate. In this case, the perversion could travel upon winding or unwinding freely, with zero torque [30]. Our present analysis assumes both κ_0 and τ_0 to be nonzero, implying that the natural state has a finite positive pitch, while the inverted helix, when unloaded, has collapsed coils. The symmetry between (+) and (−) states is broken by finite τ_0. In turn, one has to pay elastic energy when transforming (+) to (−) states: unwinding by Δn costs energy $-M_{\text{plateau}}\Delta n$, where the value of $M_{\text{plateau}} \propto -\tau_0$ [see Eq. (6)]. The quasiflatness of $M_{\text{plateau}}(n)$ in the mixed state implies that the rod acts as a *constant torque actuator*; see the Supplemental Material [32], video 5. A nice parallel can be drawn with the case where the rod is held at constant $n = 0$ and the distance z increases, as discussed in [30] in the context of a torque-free spring. In our case, the perversion turns, modulating both (+) and (−) states and keeping the torque flat. The resulting spring is then softer than the same spring in a pure + or − state, both in extension [see Fig. 2(a)] and in rotation [see Fig. 2(b)].

This apparently simple mechanical system exhibits several remarkable properties that hold significance in biology, bioinspired microrobotics [36], or mechanical engineering [37] and brings new insight even in the context of single-molecule unwinding [38]. More generally, torque plateau together with injection and annihilation snapping events are remarkable observable phenomena certainly relevant to the exploration of nature and to the design of new biomimetic devices.

The present research is a part of DynaVine action supported by the IdEX Université Paris Cité, ANR-18-IDEX-0001. We also would like to thank A. Goriely, L. Truskinovsky, and D. Bigoni for discussions.

*drazen.zanchi@u-paris.fr

[1] C. Darwin, *On the Movements and Habits of Climbing Plants* (Cambridge University Press, Cambridge, England, 1865).
[2] S. J. Gerbode, J. R. Puzey, A. G. McCormick, and L. Mahadevan, Science **337**, 1087 (2012).
[3] R. E. Goldstein, A. Goriely, G. Huber, and C. W. Wolgemuth, Phys. Rev. Lett. **84**, 1631 (2000).
[4] D. Nakane, T. Ito, and T. Nishizaka, J. Bacteriol. **202**, e00735 (2020).
[5] J. P. Canejo and M. H. Godinho, Materials **6**, 1377 (2013).
[6] P. E. S. Silva, J. L. Trigueiros, A. C. Trindade, R. Simoes, R. G. Dias, M. H. Godinho, and F. V. de Abreu, Sci. Rep. **6**, 23413 (2016).
[7] G. Kirchhoff, J. Reine Angew. Math. **56**, 285 (1859).
[8] A. E. H. Love, *A Treatise on the Mathematical Theory of Elasticity*, 4th ed. (Dover, New York, 1944).
[9] S. P. Timoshenko and J. M. Gere, *Theory of Elastic Stability*, 2nd ed. (McGraw-Hill, New York, 1961).
[10] B. Audoly and Y. Pomeau, *Elasticity and Geometry: From Hair Curls to the Non-Linear Response of Shells* (Oxford University Press, New York, 2010).
[11] A. Goriely, *The Mathematics and Mechanics of Biological Growth* (Springer Nature, New York, 2016).
[12] T. R. Strick, J.-F. Allemand, D. Bensimon, A. Bensimon, and V. Croquette, Science **271**, 1835 (1996).
[13] J. F. Allemand, D. Bensimon, R. Lavery, and V. Croquette, Proc. Natl. Acad. Sci. U.S.A. **95**, 14152 (1998).
[14] Z. Bryant, M. D. Stone, J. Gore, S. B. Smith, N. R. Cozzarelli, and C. Bustamante, Nature (London) **424**, 338 (2003).
[15] A. Sarkar, J.-F. Léger, D. Chatenay, and J. F. Marko, Phys. Rev. E **63**, 051903 (2001).
[16] C. Bustamante and S. Yan, Q. Rev. Biophys. **55**, e9 (2022).
[17] J. F. Marko and S. Neukirch, Phys. Rev. E **88**, 062722 (2013).
[18] D. E. Moulton, T. Lessinnes, and A. Goriely, J. Mech. Phys. Solids **142**, 104022 (2020).
[19] A. Goriely and S. Neukirch, Phys. Rev. Lett. **97**, 184302 (2006).
[20] T. J. Jones, E. Jambon-Puillet, J. Marthelot, and P. T. Brun, Nature (London) **599**, 229 (2021).
[21] J. Mehling, M. Diftler, M. Chu, and M. Valvo, in *Proceedings of the First International Conference on Biomedical Robotics and Biomechatronics* (IEEE, New York, 2006), pp. 690–695.
[22] V. Lutz-Bueno, S. Bolisetty, P. Azzari, S. Handschin, and R. Mezzenga, Adv. Mater. **32**, 2004941 (2020).
[23] A. F. da Fonseca and D. S. Galvão, Phys. Rev. Lett. **92**, 175502 (2004).
[24] Z. Zhou, P.-Y. Lai, and B. Joós, Phys. Rev. E **71**, 052801 (2005).
[25] L. Dai and W. Z. Shen, Nanotechnology **20**, 465707 (2009).
[26] L. Dai, K.-D. Zhu, W. Shen, X. Huang, L. Zhang, and A. Goriely, Nanoscale **10**, 6343 (2018).
[27] A. Lazarus, J. Miller, and P. M. Reis, J. Mech. Phys. Solids **61**, 1712 (2013).
[28] K. Sun and X. Mao, Phys. Rev. Lett. **127**, 098001 (2021).
[29] A. Goriely and M. Tabor, Phys. Rev. Lett. **80**, 1564 (1998).
[30] McMillen and Goriely, J. Nonlinear Sci. **12**, 241 (2002).
[31] G. Domokos and T. J. Healey, Int. J. Bifurcation Chaos **15**, 871 (2005).

[32] See Supplemental Material at http://link.aps.org/supplemental/10.1103/PhysRevLett.131.177201 for supplemental figures, videos and data.
[33] S. Kehrbaum and J. H. Maddocks, Phil. Trans. R. Soc. A **355**, 2117 (1997).
[34] L. Truskinovsky and A. Vainchtein, J. Mech. Phys. Solids **52**, 1421 (2004).
[35] E. Doedel, H. B. Keller, and J. P. Kernevez, Int. J. Bifurcation Chaos Appl. Sci. Eng. **01**, 745 (1991).
[36] M. Vogt, M. Langecker, M. Gouder, E. Kopperger, F. Rothfischer, F. C. Simmel, and J. List, Nat. Phys. **19**, 741 (2023).
[37] A. Afghoul, S. Amaravadi, A. Boumali, J. Calmeto, J. Lima, J. Lovell, S. Tinkham, K. Zemlak, and T. Staal, Oilfield Rev. **16**, 38 (2004).
[38] J. F. Marko and S. Neukirch, Phys. Rev. E **88**, 062722 (2013).